Date of publication xxxx 00, 0000, date of current version xxxx 00, 0000.

Digital Object Identifier 10.1109/ACCESS.2020.DOI

Analytical Dead-Band Compensation for ZCS Modulation Applied to Hybrid Si-SiC Dual Active Bridge

MACIÀ CAPÓ-LLITERAS[1], DANIEL HEREDERO-PERIS[1], FRANCISCO DÍAZ-GONZÁLEZ[1], MARC LLONCH-MASACHS[1], DANIEL MONTESINOS-MIRACLE[1]

[1]Centre d'Innovació Tecnològica en Convertidors Estàtics i Accionaments (CITCEA-UPC) Departament of Electrical Engineering, Universitat Politècnica de Catalunya ETS d'Enginyeria Industrial de Barcelona, C. Avinguda Diagonal, 647, Pl. 2, 08028 Barcelona, Spain

Corresponding author:Macià Capó-Lliteras (e-mail: macia.capo@upc.edu).

This work has been supported by the European Union's Horizon 2020 programme under the grant agreement number 773715.

ABSTRACT This paper proposes a triangular modulation with zero current switching (ZCS) for a hybrid Si-SiC isolated bidirectional DC-DC converter (IBDC). Three of the four legs in the IBDC operate at ZCS and use Si IGBTs, while the fourth operates at zero voltage switching (ZVS) and uses SiC MOSFET. In that case, the turn-off switching losses are concentrated regardless of the direction of the power. The main contribution of this paper resides in the proposed dead-band compensation mechanism. This dead-band compensation is crucial when addressing ZCS modulation and improves the overall efficiency of the full operating range. As a co-benefit, the proposed mix of semiconductor technologies can result in an effective cost reduction compared with a full SiC IBDC. The paper contains a detailed explanation of the implemented modulation applied to an IBDC. The paper contributes to deploy a theoretical implementation where the effect of parasitic capacitance on semiconductors during the dead-band is analytically considered. The presented method results are validated on a laboratory set-up using a 20 kW - 40 kHz hybrid Si-SiC IBDC.

INDEX TERMS Dual active bridge (DAB); Dead-band (DB); Hybrid Si-SiC; Triangular modulation; Zero current switching (ZCS).

I. INTRODUCTION

THE penetration of batteries for local storage and electric vehicles (EVs) is increasing day by day. Perspectives of EV market foreshadow an exponential growth for the following years [1], [2]. This fact also helps to promote local storage by second-life batteries, considered inappropriate for traction applications although they still have 80% of its original capacity [3].

The new electrical scenario is heading to an ecologically friendly energy system. However, this new paradigm presents technological challenges. Electronic power converters are needed to manage the energy of batteries in both directions. The capability of charging and discharging them allows offering flexibility services such as grid support, load shifting, peak shaving, among others [4], [5]. Due to safety grounds, galvanic isolation becomes mandatory according to international standards [6], especially in high power systems [7]. Moreover, power density has high importance in the automotive industry in which space and weight are limited. This also applies to dwellings in which the worth of land is continuously increasing, especially in big cities.

Dual active bridge (DAB) converter is positioning as a suitable power electronics-based component that fulfills all mentioned requirements. This isolated bidirectional DC-DC converter (IBDC) typology is mainly attractive for its power density, galvanic isolation, and bidirectional power flow capability [8]. The DAB was proposed at the beginning of 1990s [9], and it has been historically used in applications such as photovoltaic systems [10] or plug-in hybrid electric vehicles [11]. The converter typology consists of two H-bridges that connect two DC links through a high-frequency transformer, which provides the galvanic isolation. The leakage inductance current of the transformer is controlled to achieve the desired power flow.

The fact that mainly characterizes a DAB converter is its high working frequencies to reduce passive elements' weight

and size. Initially, DAB typologies operating at high frequencies were restricted to applications of few kilowatts and mid-level voltage DC-links because IGBTs semiconductors had to be used, known for their high switching losses [12]. Although synchronous rectification can be used [13], the use of IGBTs remains to be not suitable at high-frequency. The development of Wide Band-gap Semiconductors like SiC provides enhanced capabilities, such as increasing the power density and efficiency [14], [15].

Different modulation techniques for DABs have been proposed in the past, such as extended-phase-shift, dual-phase-shift (DPS), Triple Phase-Shift, and reviews comparing them have been addressed in [16], [17]. By the authors' best knowledge, all these techniques imply high control complexity. They cannot be extended to whole load range under soft-switching conditions [18], [19] and are focused on working under zero voltage switching conditions (ZVS).

This paper proposes a modulation technique based on ZCS in three of the four legs because it provides better performance than ZVS in high power DAB converters where IGBTs are commonly used [20]. ZVS turn-on can be achieved as the freewheeling diode conduces before the switch is on. However, the voltage drain-source logarithmic dependency of the parasitic capacitance makes difficult to achieve ZVS during turn-off. This fact specially penalizes the use of IGBTs because of the tail current of these devices [21], which generates switching losses [20], [22], [23]. The paper proposes a comprehensive DPS triangular modulation technique to achieve ZCS in three of the four legs of the DAB converter. The method uses the DC input and output voltage, the transformer's turn ratio and the coupling inductance value to estimate the zero current crossing in the switches. Because this inductance is small, it causes flow-back current oscillations during dead-time that increase switching conduction losses.

The paper also provides an exhaustive dead-band analysis in the DPS triangular ZCS modulation strategy. This detailed analysis is complemented with an analytically dead-band (DB) compensation proposal to reduce switching losses caused by the flow-back current oscillations. With the proposed method, switching and conduction losses can be reduced regarding theoretical modulation strategies in up to 5% according to the operation point.

This paper also proposes a hybrid Si-SiC DAB solution taking advantage of lower IGBTs cost, which has been implemented in legs that switch at zero current, avoiding that IGBT tail current generates high turn-off losses. This option optimizes costs in terms of switching devices, allowing to expend up to 3-4 times less compared to the use of a full SiC DAB.

The paper is organized as follows. Triangular technique with ZCS modulation fundamentals and its power flow equations are presented in Section II. Section III analyses in detail the dead-band, flow-back, and recirculating current effect. The modified modulation strategy avoiding dead-band and flow-back current is proposed in Section IV. Section V and VI presents the analytical enhancement analysis and the experimental validation, respectively. Finally, Section VII summarizes the conclusions obtained.

II. TRIANGULAR MODULATION TECHNIQUE WITH ZERO CURRENT SWITCHING FUNDAMENTALS

Triangular Current Modulation (TCM), which receives this name because of the transformer current shape, has already been explained in previous works as [19], [24]. However, analytical expressions as a function of the current slopes are not provided. Thus, this section aims to address a comprehensive and exhaustive analysis of the TCM case.

A. TCM BRIEF COMPARISON WITH OTHER MODULATION ALTERNATIVES

A comparison of TCM technique with the rectangular and trapezoidal options is detailed in [25]–[28]. The rectangular technique does not allow to switch under zero voltage switching conditions within a whole range of phase shift, especially in a low load range in which TCM can operate under soft-switching conditions. This fact is demonstrated in detail in [25], [26], [29], and it is based on the fact that a DAB concentrates the losses on switching losses and not on conduction losses.

The TCM is the method with the lowest losses for low power range modes [25], [26], [29], [30]. The TCM's main drawback is the triangular current shape because of the high conduction losses generated due to the high RMS value. On the bright side, TCM modulation minimizes flow-back and recirculating current, which are effects that produce conduction losses. These undesired effects are explained in Section III-B. Besides, the soft-switching operation can be achieved. Moreover, the turn-off losses can always be concentrated in the same two semiconductors, regardless of the power flow direction. Accordingly, those legs which switch under ZCS condition can be implemented by standard IGBT modules, which are cheaper than SiC semiconductors. This fact is due to the SiC market is still small compared to the IGBT-Si market for its lack of maturity [31].

B. TCM INITIAL CONSIDERATIONS

The way how TCM is implemented in the article is explained in the following lines. The modulation consists of keeping 50% of the duty cycle in all legs and shift only the second and fourth ones, holding first and third ones as masters.

Fig. 1 shows the schematic of the proposed hybrid Si-Sic Dual Active Bridge in which is detailed the converter's legs (first to fourth) and semiconductors notation used hereinafter. Sx and Nx are, respectively IGBTs and diodes of the left converter. However, Qx are IGBTs, MOSFETs at third and fourth legs, and Mx are the semiconductors' diodes. It can be seen that $S1, S2, S3, S4, Q1$, and $Q2$ are IGBTs, whereas $Q3$, and $Q4$ are SiC MOSFETs instead.

Refer to Fig. 1, n is the transformer turn ratio which is bigger than the unit and V_1 and V_2 are right and left DC link voltage, respectively. Besides, $L_{Ktr} + L_m$ describes

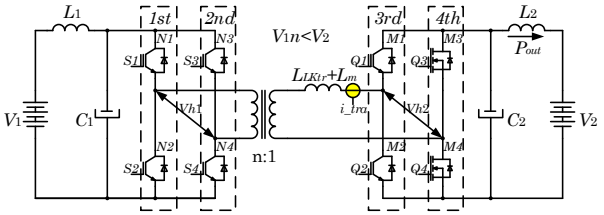

FIGURE 1. Schematic of an isolated Dual Active Bridge.

the addition of the transformer leakage inductor and the one added by design, and L_1, C_1, L_2, C_2 are the LC filters to mitigate AC components. Also, it is considered power and current towards the right side as positive.

The main restriction of TCM concerns the limitation of a boost mode operation. $V_1n \leq V_2$ considering that the leg which switches at ZVS but it does not switch at ZCS is maintained. However, note that this is not a constraint if V_1 and V_2 have a small voltage range proportionally to their rated voltage.

It is also assumed that D_1 is set as the time per unit regarding half of the switching period (ts) that lasts the current to rise up to peak value. D_2 is the period time elapsed by the current to fall up to 0 A for positive power flow. Note that D_1 and D_2 roles are exchanged for negative power flow.

Finally, the considered voltage applied to the leakage inductance is $Vh1$, $-Vh1$, $Vh2 - Vh1$, or $-(Vh2 - Vh1)$ according to the DAB switching state. From the mentioned assumptions, the positive power flow phase shift can be derived as

$$\overline{Ph_{S3+}} = (\frac{1}{2} - D_1 - D_2)ts \tag{1}$$

$$\overline{Ph_{Q3+}} = (\frac{1}{2} - D_2)ts \tag{2}$$

where $\overline{Ph_{S3+}}$ and $\overline{Ph_{Q3+}}$ mean a phase shift between $S1$ falling-edge and rising-edge of the semiconductor involved, respectively. On the contrary, negative power flow phase shift can be expressed as

$$\overline{Ph_{S3-}} = (D_1 + D_2)\, ts + \frac{ts}{2} \tag{3}$$

$$\overline{Ph_{Q3-}} = D_2 ts + \frac{ts}{2} \tag{4}$$

As an example, Fig. 2 helps to understand how the transformer (i_{tra}) and output current (i_{out}) wave shapes are obtained. Not only voltage and current are depicted but also each leg's pulse-width modulation (PWM) signals. These PWM signals are essential for deep comprehension of the dead-band effect that is addressed in Section 3. It is also important to emphasize that it can be observed how the only leg that does not switch at ZCS is the fourth in both power flow signs, positive or negative. However, ZVS in the fourth leg is achieved. Tables on the bottom of the Fig. 2 show the conduction semiconductor intervals and converter

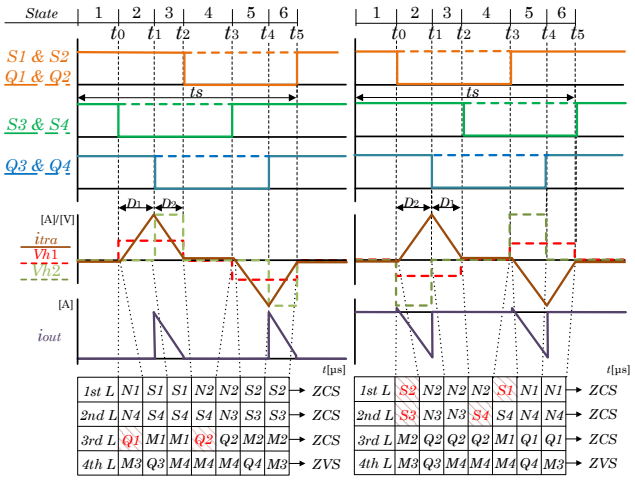

FIGURE 2. Positive power flow on the left side and negative power flow on de right side. Triangular modulation with PWM signals ($S1 - S4, Q1 - Q4$), H-bridge voltages ($Vh2, Vh1$) as well as transformer current (i_{tra}), output current (i_{out}) and, semiconductor interval conduction for each converter leg ($1stL - 4thL$).

leg ($1stL - 4thL$) following the nomenclature of Fig. 1. The MOSFET/IGBT zero-voltage turn-on is achieved if free-wheeling diode conduces before. Colored intervals of the first, second, and third leg are non zero voltage transitions but zero current instead.

Power flow analysis can be conducted once sign criteria and D_1 and D_2 meaning have been established. Analyzing the wave shape of the output current towards right DC link (i_{out}), which is depicted in Fig. 2, D_2 can be expressed as a function of P_{out} and D_1 as function of D_2 by

$$D_2 = \sqrt{\frac{P_{out}L}{V_2(V_2 - V_1n)ts}} \tag{5}$$

$$D_1 = \frac{V_2 - V_1n}{V_1n} D_2 \tag{6}$$

where P_{out} is the power flow transmitted towards right DC link, and L is the addition of transformer leakage inductance plus the inductor that has to be added by design $L = L_{LKtr} + L_m$.

Hence, the converter can be theoretically controlled as a current source in open loop mode. Therefore, D_1 and D_2 can be calculated by (5) and (6). Finally, the applied phase shift is determined by D_1 and D_2 using (1) to (4).

III. DEAD-BAND EFFECT AND FLOW-BACK CURRENT

Dead-band results in the impossibility to interchange instantaneously the on-off roles of real switching on two switches belonging to the same leg. The dead-band effect has been widely analyzed in previous publications focused on DAB converters as in [14], [32], [33], [33]–[37].

Unlike existing literature, this paper details all different switching states of TCM, taking into account the voltage and current evolution, which are not controlled during dead-band due to parasitic elements. The path followed by the current

will be highlighted for each state as well as the corresponding PWM signals. Voltages and currents of the transformer will be accordingly depicted, too.

This section presents an exhaustive explanation for positive power flow. The negative option can be derived from symmetry.

A. ANALYSIS OF SWITCHING INTERVALS

The element which causes the undesired effect during dead-band is the parasitic capacitor of semiconductors [14], [38]. When the voltage of the simultaneously switched master legs (first and third legs, see Fig. 1) have their middle point floating for neither up nor down semiconductor, their parasitic capacitors are charged or discharged. These charge/discharge processes occur according to both the initial capacitor voltage and the initial current circulating through the inductor. When the current extinguishes under that condition, the equivalent circuit constituted by the bus capacitor, the inductance, and the parasitic capacitor resonate. This resonance is a consequence of a nonfixed voltage and produces undesired currents.

Unlike the positive power flow scenario shown in Fig. 2, if the dead-band effect is taken into account, more than six states can be analyzed because of the mentioned dead-band and the parasitic capacitors of semiconductors. A total amount of fourteen different states can be considered for a single period, as can be observed in Fig. 3. This figure shows in dashed lines how voltage and current waves are modified regarding theoretical wave shapes due to dead-band and flow-black current. Fig. 4 and Fig. 5 represent the different switching states, which are treated as intervals of time in consonance with Fig. 3.

Two hypotheses are considered to facilitate the analysis interval by interval. First, it is supposed that a negative current at the beginning of the period exists. Second, it is assumed that dead-band lasts less than a ringing resonant frequency period because turn-on/off action holds the current and extinguishes the ringing. Fig. 6 depicts the current shape if the voltage on both sides of the transformer is imposed to 0 V after dead-band. On the other hand, Fig. 6 also depicts if the voltage is not held at any specific level. Thus, the ringing keeps generating, and the current cannot be controlled. In the following lines, every switching interval is explained.

As global assumptions for subsequent analysis consider that:

- The beginning of each state excludes switching action, *(*, but it is included at the end,*]*.
- When C_{Sx} or C_{Qx} are mentioned, they refer to the parasitic capacitor of the corresponding semiconductor (Sx or Qx).
- When the inductor is mentioned, it refers to the addition of the transformer leakage inductance, plus the one has to be added by design.

Interval 1 $(0 \leq t \leq t_0]$: Due to the voltage is fixed on both sides at 0 V through the fourth top semiconductors

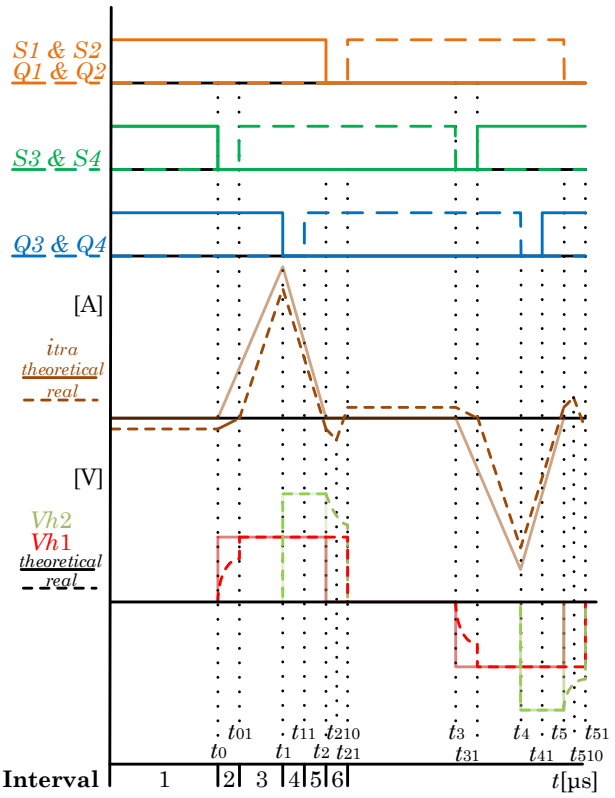

FIGURE 3. Triangular modulation considering dead-band for positive power flow. PWM signals ($S1 - S4, Q1 - Q4$), theoretical and real H-bridge voltages ($Vh2, Vh1$) as well as transformer current (i_{tra}).

$(S1, S3, Q1, Q3)$, it flows recirculating current (I_{rc}) until the following state, which is a phenomenon detailed explained in Subsection III-B.

During this interval, any present current has to be reduced as much as possible because it generates conduction losses, and no power is transferred. Besides, if the current is not about 0 A, $S3$ turn-off is not set under ZCS conditions at t_0, so more switching losses are produced. The voltage applied and current flow during this interval are detailed in Fig. 4a.

Interval 2 $(t_0 \leq t \leq t_{01}]$: Once IGBT $S3$ turns off at t_0, the midpoint of second leg is floating until t_{01}.

During this interval, the midpoint voltage depends on the state of charge. As a consequence, the voltage of C_{S3} and C_{S4}. The initial condition at t_0 is mainly defined for the negative current of the inductor, 0 V of C_{S3} and V_1 of C_{S4}. After t_0, charge of C_{S3} and discharge of C_{S4} starts. Hence, the voltage $Vh1$ increases due to the inductor's energy, a partial zero voltage switching [39] in $S4$ during turn-on is achieved. The voltage applied and current flow during this interval can be observed in Fig. 4b.

Interval 3 $(t_{01} \leq t \leq t_1]$: Once $S3$ turns off, the inductor current soars until t_1 because V_1 is applied to it. At t_1, when $Q3$ turns off is the time interval in which more switching losses are generated (analogous situation at t_4 when $Q4$ turns-off). In both mentioned instants, it must be highlighted that it is the fourth leg that switches, and it is implemented

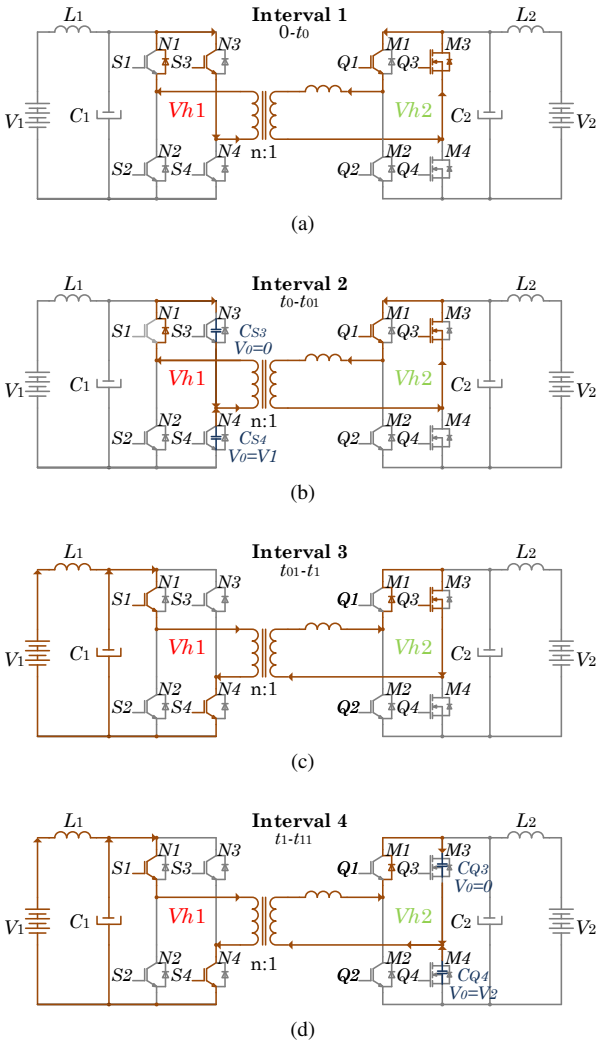

FIGURE 4. Switching states in positive rising semi-period with dead-band effect.(a) State between 0 and t_0. (b) State between t_0 and t_{01}. (c) State between t_{01} and t_1. (d) State between t_1 and t_{11}.

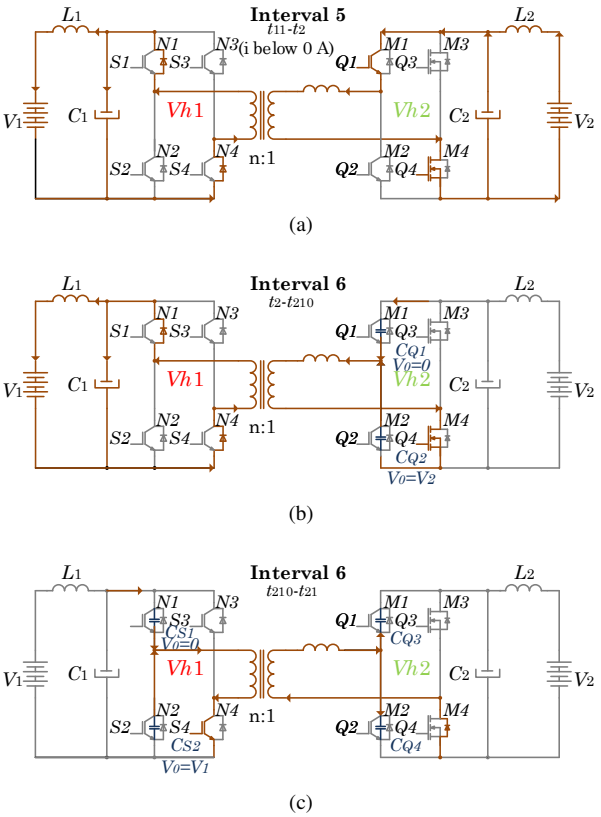

FIGURE 5. Switching states in positive falling semi-period with dead-band effect. (a) State between t_{11} and t_2. (b) State between t_{11} and t_2. (c) State between t_2 and t_{210}. (d) State between t_{210} and t_{21}.

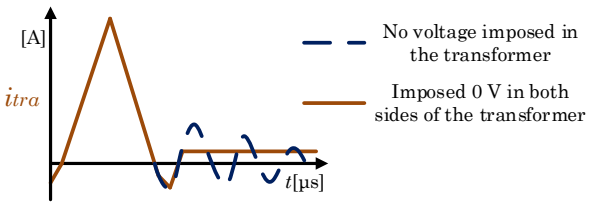

FIGURE 6. Ringing current during dead-band

with SiC MOSFETs. The voltage applied and current flow during this interval are shown in Fig. 4c.

Interval 4 $(t_1 \leq t \leq t_{11}]$: After t_1, midpoint of fourth leg is floating. Due to the amount and direction of the current, C_{Q3} is charged at $V1$ and C_{Q4} at 0 V in a short period. Therefore, diode $M4$ is forward polarized, and current starts to flow. The voltage applied and current flow during this interval is depicted in Fig. 4d.

Interval 5 $(t_{11} \leq t \leq t_2]$: Due to the diode $M4$ is forward polarized the drain-source voltage drop is of few volts (usually about 1 V). Hence, $Q4$ turns on is achieved under ZVS conditions. During $t_1 - t_2$, current drops until is 0 A because negative voltage is applied, $V_1 n - V_2$.

This analysis has been considered that $Q1$ and $Q2$ turn-off actions are set just below 0 A. This phenomenon has to be avoided because it causes a flow-back current, further explained in Section III-B. Fig. 5a illustrates the applied voltage and current flow during this interval.

Interval 6 $(t_2 \leq t \leq t_{21}]$: At t_2 the current is a bit negative when $S1$ and $Q1$ turn-off. At this moment C_{Q1} starts to charge, C_{Q2} discharges and current keeps flowing on left side through $D1$ and $D2$.

When the current extinguishes, the midpoint of the first leg is also floating. This fact produces an exchange of energy between the midpoints of first and third legs that generates a current ringing. This phenomenon lasts until $S2$, and $Q2$ turn. Thus, the midpoint voltages are determined. In this interval analysis, it has been assumed that current is positive when switches turn-on. The applied voltage and current flow during this interval can be observed in Fig. 5b and Fig. 5c, which depict the change of current sign during the interval.

The switching states of the second half period, between t_{21} and t_{51} of Fig. 3 can be addressed by horizontal symmetry among positive and negative semi-period.

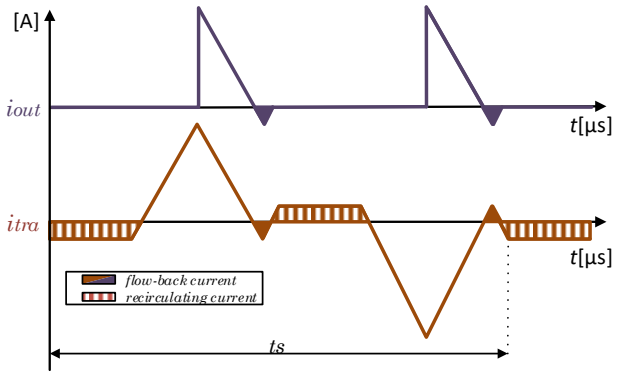

FIGURE 7. Flow-back current phenomenon for power flow to the right side.

B. FLOW-BACK AND RECIRCULATING CURRENT

On the one hand, the flow-back current phenomenon is well-known and detailed in the literature, as shown in [13], [40], [41]. Flow-back current is described as the current, which flows on the opposite of the desired side. Considering this paper's sign criteria, flow back current is produced when there is negative power flow transiently, whereas positive power flow is set or vice-versa. This undesired current behavior has to be avoided due to the correlation with rising losses. On switching strategy explained in Section II, this phenomenon occurs during the oscillation while downing the current it drops crossing 0 A until it comes back to cross 0 A again. In Fig. 7, this undesired behavior is depicted in the colored zones. Fig. 5b exemplifies a switching state with the flow-back current in which power flows to V_2 and not from V_1.

On the other hand, the recirculating current is the current which flows through the transformer, but it is transferred to neither $V1$ nor $V2$ DC links. This phenomenon occurs when $S1, S3, Q1$, and $Q3$ or $S2, S4, Q2$, and $Q4$ are closed simultaneously. Recirculating current occurs during intervals $(0 - t_0)$, which is depicted in Fig. 4a, and in colored vertical stripes in Fig. 7. It has to be highlighted that due to the low parasitic resistance, the power dissipation is not appreciable during these short periods, and the current does not extinguish.

IV. PROPOSAL OF SWITCHING STRATEGY MODIFICATION AVOIDING DEAD-BAND EFFECT

This section presents an analytical compensation to enhance the current behavior avoiding the flow-back and the recirculating current effect described in Section III. Moreover, this proposal contributes to reducing both switching and conduction losses.

A. ANALYTICAL STRATEGY MODULATION MODIFICATION

The modification of the theoretical modulation is presented in three different sections taking into account how the current shape is modified, which consequences have the modification for the power set-point calculation, and the power losses for both theoretical and proposed modulation.

1) Conditioning switching states to avoid current ringing

The modulation strategy modification aims to avoid current ringing by switching first and third legs earlier to do not float, and the inductor does not work under discontinuous mode. If current reaches 0 A during DB is noncontrollable and ringing starts, so I_{rc} cannot be inhibited. This phenomenon has been observed in Fig. 6. Hence, switching states of first and third legs $(S1, S2, Q1, Q2)$ are put forward, matching DB's end at 0 A and not at the beginning.

This modification on the phase shift and its consequences are depicted in Fig. 8. It can be observed that current switches just before DB (I_{DB}) is addressed under ZVS conditions but not under ZCS conditions. I_{rc} is inhibited, so conduction losses are reduced. Besides, switching losses due to the 0 A at the beginning of the following semi-period.

As can be seen, the area is reduced compared to the original power set-point. Fig. 8 also shows three different current slopes. As it was in original mode, current slope during D_1 is proportional to $\alpha\ V_1$, and to $\alpha(V_2 - V_1 n)$ at D_2. However in that case, during dead-band, V_2 is applied and $\alpha\ (V_2 - V_1 n)$ only during

$$D_2 - DB - D_p \tag{7}$$

where DB is dead-band per unit, and D_p is the period per unit in which, unlike theoretical modulation, during the modified strategy proposed, it does not flow current. On the one hand, DB must be greater than [42]

$$DB \geq t_{fall} + (t_{delay\,off} - t_{delay\,on}) \tag{8}$$

where t_{fall} is the time that lasts the semiconductor between voltage starts to rise from the forward diode voltage up to DC link voltage. Besides, $(t_{delay\,off}$ and $t_{delay\,on}$ are the times between the driver signal applied and the semiconductor voltage starts to rise or drop, respectively. Often, a circuit safety margin of twice the minimum DB is applied.

On the other hand, D_p represent the triangle base of the power which in proposed modified modulation is not transferred regard theoretical strategy, and it can be derived as

$$D_p = \left(\frac{1}{1 - \frac{V_1 n}{V_2}}\right) DB\ ts \tag{9}$$

Considering Fig. 5a, if S_1 and Q_1 turn-off when current is still positive, current behavior is different from which is presented in Section III-A. In that case, the following switching state would be how it is presented in Fig. 9. It can be deduced that the voltage applied to the inductor is $-V_2$, and the dropping slope is higher than $V_2 - V_1 n$ due to $V_1 n \leq V_2$.

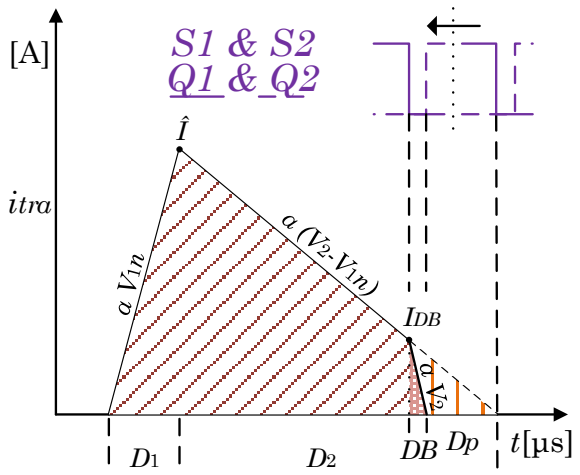

FIGURE 8. Positive semi-period transformer current for positive power flow with modulation modification. Advance of fist and third legs switching states are depicted ($S1, S2, Q1, Q2$), as well as peak current ($\widehat{I}$), current just before dead-band (DB) (IDB) and the three different current slopes ($\alpha V_1 n, \alpha(V_2 - V_1 n)$ *and* αV_2))

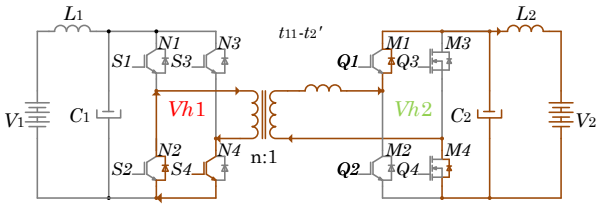

FIGURE 9. Switching state after Fig. **??** if $S1$ and $Q1$ are turned off and the inductor current is still positive.

2) Power set-point recalculation

Analyzing the wave shape from Fig. 8, it can be deduced that master legs (first and third) have to be put forward or second and fourth legs have to be shifted with delay $DB+D_p$ so as to start and finish the triangle at 0 A. If V_1 and V_2 are constants, this adding phase shift, PH^+, is also constant, and it follows

$$PH^+ = (\frac{1}{1-\frac{V_1 n}{V_2}} - 1)DB\ ts \tag{10}$$

D_2 as a function of P_{out} must be recalculated to generated the corrected power set-points because the wave shape has changed

$$\begin{aligned} P_{out_{D_2}} =& \frac{V_2}{L}[V_2 - V_1 n \cdot D_2^2 ts \\ &+ DB \cdot ts(2 \cdot V_2 D_2 + V_2 DB \cdot ts)] \end{aligned} \tag{11}$$

where relationship between $D2$ and $D1$ keeps following (6). In this case, D_1 and D_2 expressions as function of P_{out} become more complex so as to be solved each scan cycle of microprocessor. For this reason, in order to get an easier computing calculation, D_1 and D_2 are derived by (5) and (6). If these D_1 and D_2 are applied after adding phase shift calculated in (10), the power obtained corresponds to the set-point less the power corresponding to the triangular area, P_{sub}, from Fig. 8 which base is D_p and its height is I_{DB}. This subtracted power, P_{sub}, is constant if $V1$, $V2$ and DB, are constant and it can be derived as

$$P_{sub} = \frac{V_2^2}{L} DB^2 ts(\frac{1}{1-\frac{V_1 n}{V_2}} - 1) \tag{12}$$

Therefore, it is only necessary to set a reference as it was done before and add P_{sub} term.

3) Analytical power losses calculation

Conduction and switching losses have to be taken into account. The shape of current that circulates through the semiconductors, so RMS values determine conduction losses. Hereinafter I is the RMS current and for positive power flow when modulation is affected by dead-band can be derived as:

$$I_{Ss} = \sqrt{\frac{\widehat{I_I}^2}{3}(D_1 + D_2) + I_{rc}^2(1 - (D_1 + D_2))} \tag{13}$$

$$I_{Ml3} = \sqrt{\frac{\widehat{I_{II}}^2}{3}(D_1 + D_2) + I_{rc}^2(1 - (D_1 + D_2))} \tag{14}$$

$$I_{Ql4} = \sqrt{\frac{\widehat{I_{II}}^2}{3} D_1} \tag{15}$$

$$I_{Ml4} = \sqrt{\frac{\widehat{I_{II}}^2}{3} D_2 + I_{rc}^2(1 - (D_1 + D_2))} \tag{16}$$

where Ss are the IGBTs of left H-bridge, $Ml3$ the diodes of the third leg, $Ml4$ the diodes of the fourth leg and $Ql4$ are the MOSFETs of the fourth leg. Besides, $\widehat{I_I}$ and $\widehat{I_{II}}$ are peak current of primary and secondary respectively.

On the contrary, RMS current for proposed modulation can be derived as (17-20).

$$I_{Ql4} = \sqrt{\frac{\widehat{I_{II}}^2}{3} D_1} \tag{19}$$

$$I_{Ml4} = \sqrt{\frac{\widehat{I_{II}}^2}{3} (D_2 - D_p - DB)} \tag{20}$$

Hence, the total semiconductor power losses can be obtained and compared between the theoretical strategy with the dead-band effect and the proposed strategy. In Section VI, the outcomes for the DAB used are presented.

The modified strategy has more capability to transfer power for a given converter. This fact can be analyzed geometrically. The modified strategy is a specific case of trapezoidal modulation, which, as mentioned in Section II, can transfer more power than the triangular technique. The modulation strategy proposed in this section modifies the triangular technique. It gets an unsymmetrical trapezoidal shape that minimizes dead-band and flow-back current effect and conduction and switching losses. Regarding the Fig. 8, I_{DB} is a fixed value if dead-band is not modified and V_2 does

not change. I_{DB} should be as less as possible to have the minimum switching losses. This fact implies the necessity to deploy the minimum possible dead-band, conditioned by the MOSFET or IGBT's rising and falling edge.

V. THEORETICAL ENHANCEMENT ANALYSIS

Previous sections have presented a series of effects such as dead-band, flow-back, recirculating, or ringing currents that degrades the ideal performance of a DAB operated under ZCS-TCM. This section aims to analyze attainable enhancement theoretically margin when the proposed modulation of Section IV is adopted.

Expressions (17) to (20) are needed to calculate RMS current, as well as power losses for both theoretical with dead-band effect and the proposed modulation. For the addressed analysis, the power transfer assumed is 0-10 kW, switching frequency is 40 kHz, rated current I_{out} is 25 A, both DC-links are 800 V, and DB is set at 0.6 μs.

A. RMS CURRENT (I_{RMS}) ANALYSIS VERSUS RECIRCULATING (I_{RC}) CURRENT AND OUTPUT POWER (P_{OUT})

The RMS current (I), which is the main parameter to calculate conduction losses, not only depends on the peak current but also the I_{rc}. This subsection analyses how I_{rc} produces a rising of conduction losses as a function of the P_{out}.

The peak current ($\widehat{I}$), for proposed modulation, is slightly bigger than the peak current of theoretical modulation for the same given power. However, RMS current is not bigger for all output power, P_{out}, or for all recirculating current, I_{rc}. It depends on the level and duration of the I_{rc} current, which effect was explained in Section III-B. For the low rate of power, the recirculating current has a worse outcome due to it lasts (1-$D1$-$D2$) where ($D1$+$D2$) is the base of the current with a triangular shape. Fig. 10 shows two 3-D surfaces that link the I_{RMS} current with both I_{rc} and P_{out} magnitudes for both ZCS-TCM with (solid) and without (semi-transparent) dead-band compensation. In this figure can be deduced which I_{rc} produces a rise of I_{RMS} in theoretical modulation that makes equal I_{RMS} of the proposed modulation, i.e. when both surfaces cross-over. Above this I_{rc} the I_{RMS} current is bigger in theoretical modulation with dead-band effect. As it can be seen in Fig. 10, I_{RMS} is slightly lower in high load conditions for theoretical modulation, but it can change due to the dependency of I_{rc} which level is not controllable since it is set during DB when neither voltage nor current can be held. On the contrary, proposed modulation assures low I_{RMS} under low load conditions. As it can be observed in Fig. 10, in some cases, I_{RMS} is reduced four times which represents 16 times fewer conduction losses.

TABLE 1. Converter specifications

Rated power	P_{out}	20	kW
Rated power base	$1PU$	20	kW
Switching frequency	fs	40	kHz
DC voltage range high side	$V1$	0-800	V
DC voltage range low side	$V2$	0-800	V
DC rated current	I_{out}	25	A
Dimensions		440x174x170	mm
Power density		1.54	kW/dm^3

B. POWER LOSS IMPROVEMENT ANALYSIS VERSUS RECIRCULATING CURRENT AND OUTPUT POWER

Moreover, as it was mentioned in Section IV-A, proposed modulation also reduces switching losses. Total semiconductor power losses of the used DAB are presented in Fig. 11 for theoretical and modified strategies. The output power range of 0.5 PU (0-10 kW) for $V_2/V_1 = 3/2$ is the converter's load range that TCM is the most efficient switching strategy. It can be seen that when I_{rc} current is higher than about 9 A, the losses produced by theoretical modulation rise linearly concerning the proposed modulation. For instance, in Fig. 11 when I_{rc} reaches 15 A, it can be observed that total power losses are reduced by 50%.

VI. EXPERIMENTAL RESULTS

The proposals presented in the article have been validated by means of the hybrid Si-SiC prototype shown in Fig. 12. The main converter's specification are summarized in Table 1. Besides, this prototype and the obtained results have been used to develop the first industrial version for the RESOLVD project (European Union's Horizon 2020, LCE-01-2016-2017) that can be seen in Fig. 13.

This section aims to demonstrate using this hardware the dead-band, the flow-back, and the recirculating or ringing current effect. The section also allows proving experimental results that applying the analytical expressions and methods proposed in Section IV are valid, and they enhance the theoretical operation.

A. HYBRID SI-SIC DAB DETAILS

One of this paper's proposals is to present a hybrid Si-SiC DAB in terms of cost sensitivity. As mentioned in Section II,

$$I_{Ss} = \sqrt{\frac{\widehat{I_I}^2}{3} D_1 + \frac{(\widehat{I_I}^2 + {I_{DB}}^2 + I_{DB}\widehat{I_I})}{3}(D_2 - D_p - DB) + \frac{{I_{DB}}^2}{3} DB} \tag{17}$$

$$I_{Ml3} = \sqrt{\frac{\widehat{I_{II}}^2}{3} D_1 + \frac{(\widehat{I_{II}}^2 + {I_{DB}}^2}{+} I_{DB}\widehat{I_{II}})3(D_2 - D_p - DB) + \frac{{I_{DB}}^2}{3} DB} \tag{18}$$

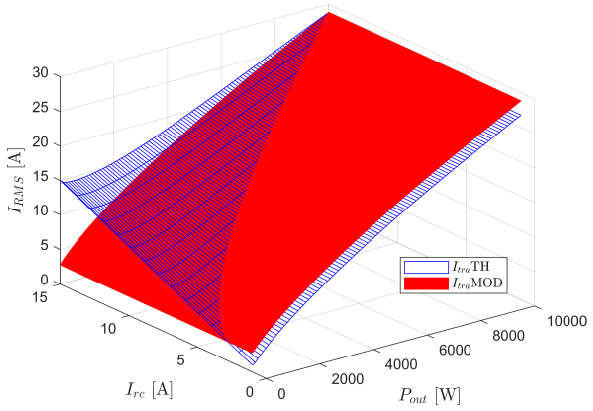

FIGURE 10. Transformer current I_{RMS} as function of transmitted power (P_{out}) and recirculating current (I_{rc}) for theoretical modulation with dead-band effect $(I_{tra}\mathrm{TH})$ and for the proposed modulation $(I_{tra}\mathrm{MOD})$

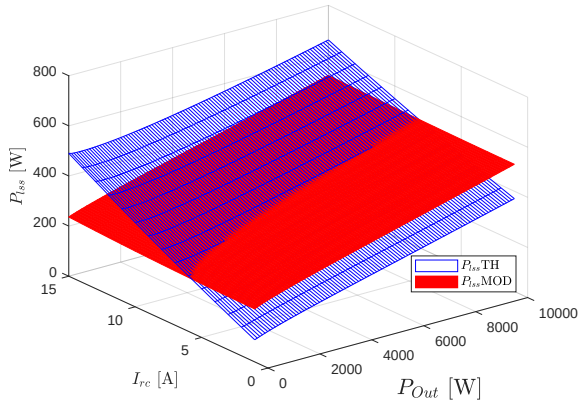

FIGURE 11. Converter power losses (P_{lss}) as function of transmitted power (P_{out}) and recirculating current (I_{rc}) for theoretical modulation with dead-band effect $(P_{lss}\mathrm{TH})$ and for the proposed modulation $(P_{lss}\mathrm{MOD})$

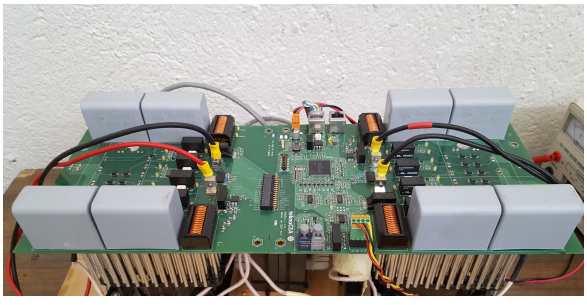

FIGURE 12. Pictures of the converter.

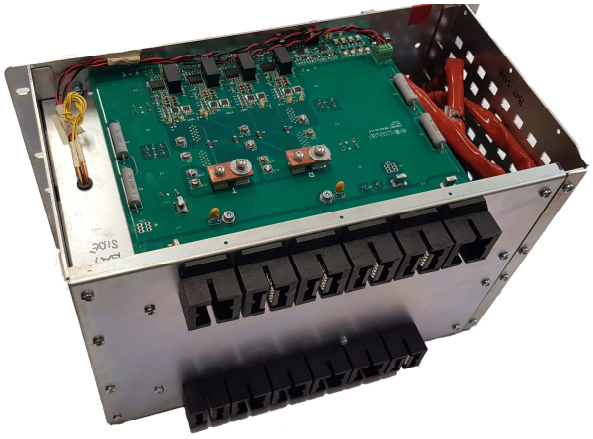

FIGURE 13. Pictures of the second prototype used in RESOLV project

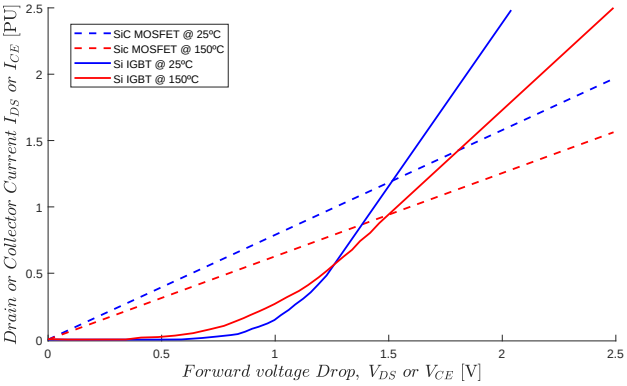

FIGURE 14. Voltage drop comparison between SiC MOSFET and Si IGBT in PU where the base is rated current

.

those legs that switch under the ZCS condition can be implemented by adopting standard IGBT modules because of the lower price than SiC MOSFETs. The recent cost analysis, 1200V SiC MOSFET vs. Silicon IGBT [31], analyzes sixteen devices from seven different manufacturers concludes that *'The SiC MOSFET Market is Still Small Compared to that for Si IGBTs due to Lack of Maturity and High Cost'*.

It is vastly presented in the literature [43], [44], [44] that for the same blocking voltage and rated current, SiC MOSFETs has about 4 to 5 times fewer switching losses than SiC, but they have similar conduction losses at rated current. Based on existing literature, this behavior is represented in Fig. 14. Thus, considering that in the presented modulation IGBTs switch under zero current condition, switching losses are almost inhibited. Therefore, SiC MOSFETs and Si IGBTs generate similar losses for semiconductor rated current in this application. The deployed semiconductors of the DAB are 6MBI50VA-120-50 Si IGBTs and CCS050M12CM2 SiC MOSFETs modules. Both switching technologies are selected to have the same package and blocking voltage of 1200 V. Although they have approximately the same conduction losses at 40 A and 150°C the switching losses of the Si

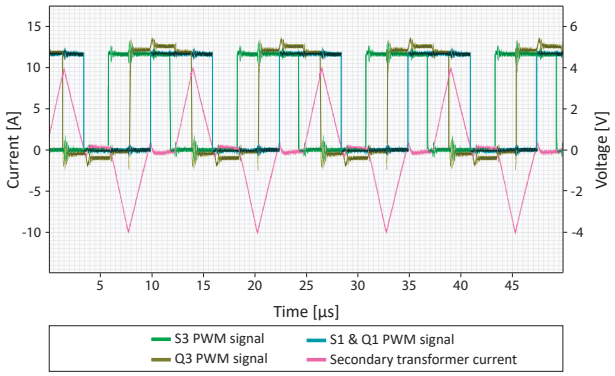

FIGURE 15. Positive power flow in triangular modulation. PWM signals and current of transformer. Where, triangular wave is secondary transformer current, square wave with first rising slope is $S3$ pwm signal, the second one is $Q3$ pwm signal and the last is $S1$ that corresponds to $Q1$ signal too.

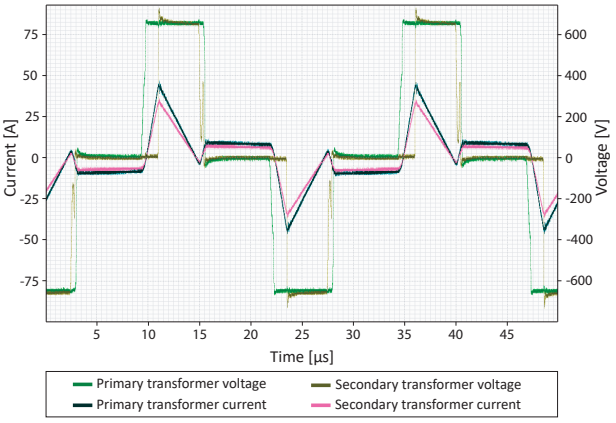

FIGURE 16. Undesired effects on transformer voltages and currents. Where lower triangular wave shape is secondary transformer current, the bigger is the primary transformer, square wave shape with first rising slope is primary transformer voltage, and the other one corresponds to the secondary transformer voltage.

module are about 4 to 5 times higher than in the SiC case. Nevertheless, Si devices are around 3 to 4 times cheaper than SiC. As a reference, consider that the cost for the same distributor of 6MBI50VA-120-50 is around 90 € and de cost of CCS050M12CM2 is around 380 €. However, the converter can operate at 40 kHz using IGBTs in ($S1$, $S2$, $S3$, $S4$, $Q1$, and $Q2$) thanks to switching under ZCS. Note that the usual case for the power level considered of 20 kW is about 20 kHz if air-cooled.

Furthermore, it has to be taken into account that the chosen semiconductors impose the minimum dead-band. In this case the slowest is IGBT technology, and the DB is set at 0.6 μs, which represents 2.4% of the 25 μs period (40 kHz).

Fig. 15 shows the PWM signals of the switching strategy for positive power flow, previously depicted in Fig. 2. Triangular wave corresponds to the transformer current. The first rising edge is the $S3$ signal, the second is $Q3$, and the last is $S1$ that corresponds to the $Q1$ signal, too. It can be observed that $Q3$ is the only one that does not switch at zero current, but turn-on zero voltage instead. Turn-off losses of $Q3$ are minimized since the semiconductor is a SiC MOSFET, and the tail current of the IGBTs is avoided [21].

B. EXPERIMENTAL CURRENT ANALYSIS

As it has been introduced in Sections III and IV, several effects can affect substantially the performance of a DAB operated under ZCS-TCM.

Fig. 16 shows the primary and secondary voltages and currents under standard ZCS-TCM. This oscilloscope capture shows the effects of dead-band, flow-back, recirculating, or ringing current effects explained in Section III-B. Each of these effects can be identified if Fig. 16 is compared with Fig. 3 and Fig. 6. The voltage can be observed how primary rises during dead-band, getting a partial zero voltage switching. Secondary voltage drops and rings during dead-band, whereas primary holds the voltage until after dead-band. This behavior produces a negative effect on the current as well. As mentioned in Section IV, the current ringing depends on the inductor current during dead-band, but mainly on the energy stored in the parasitic capacitors of the semiconductors. It is known that the energy storage of a capacitor has a quadratic dependency on the voltage applied. Hence, the higher the DC voltage is, the more ringing during dead-band results. In Fig. 16, the $V1$ and $V2$ DC bus voltages are 650 V, and the undesired ringing effect can be observed. It must highlight the fact that even if the switching is done under 0 A, the current rises in an uncontrolled way. After dead-band, in this case, IGBTs of legs first and third switch after dead-band at about 9 A. This current is nonadmissible that excessive conduction losses and forces that the following state has to be done under hard-switching conditions.

Fig. 17 shows the difference between conventional ZCS-TCM strategy described in Section II, and the proposed in Section IV which takes into account dead-band effect. Both pictures show the bottom and top driver's first leg's signal, which fixes the current when 0 V is applied to the inductor (L). In Fig. 17a, it can be seen that after a downslope current, it does not hold constant at 0 A. Actually, it rebounds until the complementary driver turns-on. Nevertheless, in Fig. 17b, it can be observed that the first leg driver turns-off is addressed time before, (described by (10)), and the complementary turn-on coincides at 0 A. Thus, the current rebound is inhibited. Actually, the shown triangular current wave remains at 0 A, while 0 V is applied to the inductor.

C. EXPERIMENTAL POWER LOSSES AND EFFICIENCY ANALYSIS

As it has been analyzed in Section V-B power losses depend on I_{rc} and P_{out}. Experimental results are obtained in the laboratory set-up. The parasitic elements of the converter generate a I_{rc} of 9 A. Fig. 18 shows analytical results which is a section plane (P_{lss}), (P_{out}) of Fig.11, and also experimental results $(ExP_{lss}\text{TH})$ and $(ExP_{lss}\text{MOD})$ are shown. It can be observed from Fig.18 that experimental results correspond to the analytical analysis. Moreover, it

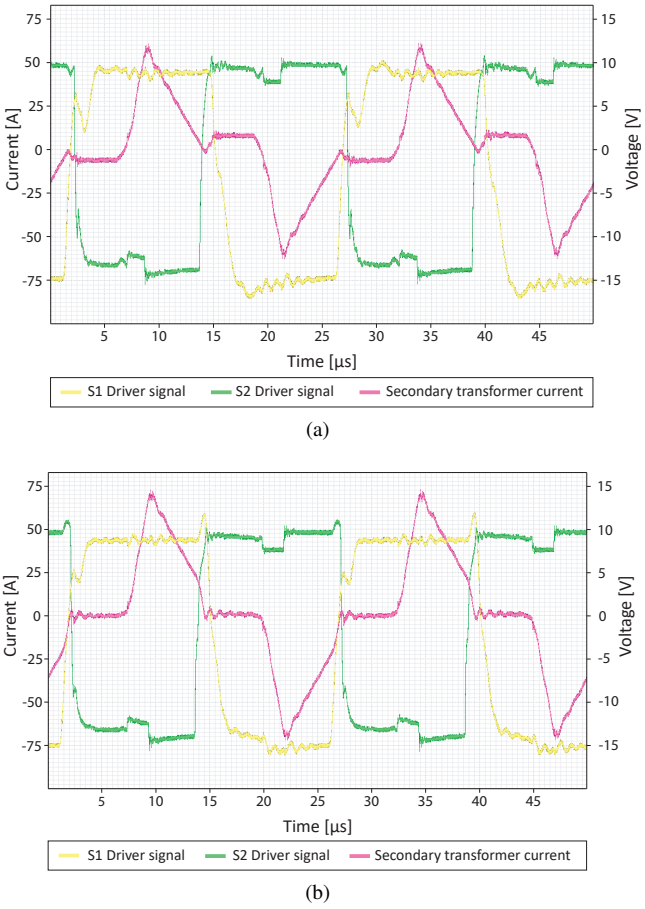

FIGURE 17. Current shape with both methods and driver signals of leg 1. Square wave shape with first rising slope corresponds to S1 driver signal, and the second one corresponds to S2 driver signal. Triangular wave is secondary transformer current. (a) Secondary current shape with no dead-band correction (b) Secondary current shape with dead-band correction.

must be highlighted that at I_{rc} of 9 A, proposed modulation generates fewer losses in the interval of 0.5 PU that is the load range of the converter in which TCM is the most efficient switching strategy.

Finally, analytical and experimental efficiency for theoretical (Eff_{lss}TH, $ExEff_{lss}$TH) and proposed modulation (Eff_{lss}MOD, $ExEff_{lss}$MOD) are shown in Fig.19. As shown in analytical and experimental in accordance, the proposed modulation has better efficiency at low load range up to 1.5%. The efficiency difference decreases at higher P_{out} due to the RMS current increments as it has been shown in Fig. 10. The improvement of the efficiency with proposed modulation depends on the I_{rc}, as shown in Fig. 11. This I_{rc} is difficult to predict because it depends on voltage operation, and parasitic capacitance and inductance. Proposed modulation removes this uncertainty and facilitates the losses analysis.

VII. CONCLUSION

This paper presents an improved switching triangular control DAB strategy to overcome undesired current shapes and larger losses considering the dead-band effect. The phase

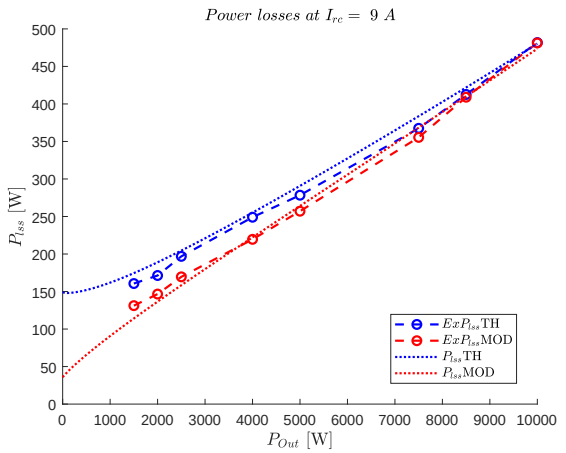

FIGURE 18. Converter power losses (P_{lss}) as function of transmitted power (P_{out}) for 9 A of recirculating current (I_{rc}) for theoretical modulation with dead-band effect (P_{lss}TH) and for the proposed modulation (P_{lss}MOD) as well as the corresponding results obtained (ExP_{lss}TH) and (ExP_{lss}MOD).

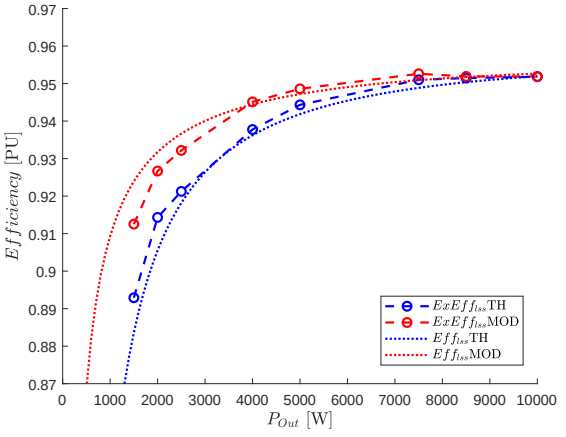

FIGURE 19. Converter efficiency as function of transmitted power (P_{out}) for 9 A of recirculating current (I_{rc}) for theoretical modulation with dead-band effect (P_{lss}TH) and for the proposed modulation (P_{lss}MOD) as well as the corresponding results obtained (ExP_{lss}TH) and (ExP_{lss}MOD).

shift has been deduced on both power flow directions. Moreover, current and voltage waveforms, and driver signals, have been depicted, providing a comprehensive way to understand the ideal behavior under the triangular modulation strategy. It has been shown that six out of eight semiconductors operate under ZCS conditions, concentrating the turn-off switching losses in the same leg regardless of the direction of the power flow. Thus, it makes it feasible to use cheaper semiconductor technology for those that work under soft-switching conditions. A hybrid Si-SiC DAB is proposed as the preferred hardware option. However, it is possible to switch at 40 kHz, the full converter even using Si IGBT switches for rated currents of 25 A and blocking voltages of 1200 V.

The paper has demonstrated that dead-band, flow-back, and recirculating current compensation is relevant to achieve optimal performance in a DAB operating under zero current

switching triangular modulation strategy. Each switching state has been comprehensively explained and depicted to obtain a clear understanding of the undesired effects. The proposed improvements on the triangular modulation allow reducing both switching and conduction losses regarding the theoretical ones. The potential in loss power reduction and output current has been studied theoretically, deducing that reductions losses can be achieved according to the output operation point. Experimental efficiencies are proved accordingly with the theoretical study in a laboratory set-up, and 1.5% efficiency increment is achieved.

All the mentioned proposals and DB effects have been validated in a 20 kW-40 kHz hybrid Si-SiC DAB.

REFERENCES

[1] D. Pelegov and J. Pontes, "Main Drivers of Battery Industry Changes: Electric Vehicles—A Market Overview," *Batteries*, vol. 4, no. 4, p. 65, 2018.

[2] D. Bresser, K. Hosoi, D. Howell, H. Li, H. Zeisel, K. Amine, and S. Passerini, "Perspectives of automotive battery R&D in China, Germany, Japan, and the USA," *Journal of Power Sources*, vol. 382, no. February, pp. 176–178, 2018.

[3] L. C. Casals, B. Amante García, and C. Canal, "Second life batteries lifespan: Rest of useful life and environmental analysis," *Journal of Environmental Management*, vol. 232, no. November 2018, pp. 354–363, 2019.

[4] O. Laribi, P. Wiest, and K. Rudion, "Optimal Dimensioning and Operation of a Grid-Supporting Energy Storage System," 2017.

[5] E. Serban, M. Ordonez, and C. Pondiche, "Beyond Standards," *IEEE Transactions on Power Electronics*, vol. 32, no. 1, pp. 298–309, 2017.

[6] C. Visvikis, "EVS26 Safety considerations for electric vehicles and regulatory activities," no. 129, 2014.

[7] D. Das, N. Weise, K. Basu, R. Baranwal, and N. Mohan, "A bidirectional soft-switched DAB-based single-stage three-phase AC-DC converter for V2G application," *IEEE Transactions on Transportation Electrification*, vol. 5, no. 1, pp. 186–199, 2019.

[8] S. Shao, H. Chen, X. Wu, J. Zhang, and K. Sheng, "Circulating Current and ZVS-on of a Dual Active Bridge DC-DC Converter: A Review," *IEEE Access*, vol. 7, pp. 50 561–50 572, 2019.

[9] R. W. A. A. D. Doncker, "A Three-phase Soft-Switched Applications / I = q," vol. 27, no. 1, 1991.

[10] Y. Shi, R. Li, Y. Xue, and H. Li, "Optimized Operation of Current-Fed Dual Active Bridge DC-DC Converter for PV Applications," *IEEE Transactions on Industrial Electronics*, vol. 62, no. 11, pp. 6986–6995, 2015.

[11] L. Xue, Z. Shen, D. Boroyevich, P. Mattavelli, and D. Diaz, "Dual Active Bridge-Based Battery Charger for Plug-in Hybrid Electric Vehicle with Charging Current Containing Low Frequency Ripple," *IEEE Transactions on Power Electronics*, vol. 30, no. 12, pp. 7299–7307, 2015.

[12] S. Hazra, A. De, L. Cheng, J. Palmour, M. Schupbach, B. A. Hull, S. Allen, and S. Bhattacharya, "High Switching Performance of 1700-V, 50-A SiC Power MOSFET over Si IGBT/BiMOSFET for Advanced Power Conversion Applications," *IEEE Transactions on Power Electronics*, vol. 31, no. 7, pp. 4742–4754, 2016.

[13] S. Luo and F. Wu, "Hybrid Modulation Strategy for IGBT-Based Isolated Dual-Active-Bridge DC-DC Converter," *IEEE Journal of Emerging and Selected Topics in Power Electronics*, vol. 6, no. 3, pp. 1336–1344, 2018.

[14] Z. Wang and A. Castellazzi, "Device loss model of a fully SiC based dual active bridge considering the effect of synchronous rectification and deadtime," *Proceedings - 2017 IEEE Southern Power Electronics Conference, SPEC 2017*, vol. 2018-Janua, pp. 1–7, 2018.

[15] H. Akagi, S.-i. Kinouchi, and Y. Miyazaki, "Bidirectional Isolated Dual-Active-Bridge (DAB) DC-DC Converters Using 1.2-kV 400-A SiC-MOSFET Dual Modules," *CPSS Transactions on Power Electronics and Applications*, vol. 1, no. 1, pp. 33–40, 2017.

[16] B. Zhao, Q. Song, W. Liu, and Y. Sun, "Overview of dual-active-bridge isolated bidirectional DC-DC converter for high-frequency-link power-conversion system," *IEEE Transactions on Power Electronics*, vol. 29, no. 8, pp. 4091–4106, 2014.

[17] C. Calderon, A. Barrado, A. Rodriguez, P. Alou, A. Lazaro, C. Fernandez, and P. Zumel, "General Analysis of Switching Modes in a Dual Active Bridge with Triple Phase Shift Modulation," *Energies*, vol. 11, no. 9, p. 2419, 2018.

[18] I. Skouros, A. Bampoulas, and A. Karlis, "A bidirectional dual active bridge converter for V2G applications based on DC microgrid," *2018 13th International Conference on Ecological Vehicles and Renewable Energies, EVER 2018*, pp. 1–9, 2018.

[19] F. Krismer, J. Biela, and J. W. Kolar, "A comparative evaluation of isolated bi-directional DC/DC converters with wide input and output voltage range," *Conference Record - IAS Annual Meeting (IEEE Industry Applications Society)*, vol. 1, no. c, pp. 599–606, 2005.

[20] A. Pal and K. Basu, "A zero-current-switched PWM full bridge DC-DC converter," *2019 IEEE Energy Conversion Congress and Exposition, ECCE 2019*, no. c, pp. 6424–6429, 2019.

[21] H. K. Y. Iwasaki, M. Chounabayashi, M. Nakazawa, S. Iwamoto, Y. Oonishi, M. Hori and O. Ikawa, "Fuji increases power density with SiC and new packaging technologies," p. 2017, 2017.

[22] J. M. Zhang, X. G. Xie, X. K. Wu, and Z. Qian, "A novel zero-current-transition full bridge DC-DC converter," *Conference Proceedings - IEEE Applied Power Electronics Conference and Exposition - APEC*, vol. 2, pp. 673–677, 2005.

[23] X. Zhang, H. S. Chung, X. Ruan, and A. Ioinovici, "A ZCS full-bridge converter without voltage over-stress on the switches," *2009 IEEE Energy Conversion Congress and Exposition, ECCE 2009*, pp. 1991–1998, 2009.

[24] G. Ortiz, C. Gammeter, J. W. Kolar, and O. Apeldoorn, "Mixed MOSFET-IGBT bridge for high-efficient medium-frequency dual-active-bridge converter in solid state transformers," *2013 IEEE 14th Workshop on Control and Modeling for Power Electronics, COMPEL 2013*, pp. 1–8, 2013.

[25] N. Hou and Y. Li, "Overview and Comparison of Modulation and Control Strategies for Non-Resonant Single-Phase Dual-Active-Bridge dc-dc Converter," *IEEE Transactions on Power Electronics*, vol. 35, no. 3, pp. 1–1, 2019.

[26] J. Everts, J. Van Den Keybus, F. Krismer, J. Driesen, and J. W. Kolar, "Switching control strategy for full ZVS soft-switching operation of a dual active bridge AC/DC converter," *Conference Proceedings - IEEE Applied Power Electronics Conference and Exposition - APEC*, pp. 1048–1055, 2012.

[27] H. Chan, "An extended load range ZCS-ZVS bi-directional phase-shifted DC-DC converter," no. 475, pp. 74–79, 2005.

[28] F. Krismer, S. Round, and J. W. Kolar, "Performance optimization of a high current dual active bridge with a wide operating voltage range," *PESC Record - IEEE Annual Power Electronics Specialists Conference*, pp. 1–7, 2006.

[29] N. Schibli, "EPFL_TH2220.pdf," Ph.D. dissertation, 2000.

[30] F. Krismer and J. W. Kolar, "Closed form solution for minimum conduction loss modulation of DAB converters," *IEEE Transactions on Power Electronics*, vol. 27, no. 1, pp. 174–188, 2012.

[31] L. G. Barbarini Elena, "1200V Silicon IGBT vs SiC MOSFET Comparison 2018 Complete Teardown Report," System Plus Consulting, Tech. Rep. September, 2018.

[32] J. Li, Z. Chen, Z. Shen, P. Mattavelli, J. Liu, and D. Boroyevich, "An adaptive dead-time control scheme for high-switching-frequency dual-active-bridge converter," *Conference Proceedings - IEEE Applied Power Electronics Conference and Exposition - APEC*, pp. 1355–1361, 2012.

[33] J. I. Itoh, K. Kawauchi, and H. Watanabe, "Non-linear Dead-time Error Compensation Method of Dual Active Bridge DC-DC Converter for Variable DC-bus Voltage," *6th IEEE International Conference on Smart Grid, icSmartGrids 2018*, pp. 208–213, 2019.

[34] J. Hu, Z. Yang, and R. W. De Doncker, "A Comprehensive Dead-Time Compensation Method for a Three-Phase Dual-Active Bridge Converter with Hybrid Modulation Schemes," *2018 International Power Electronics Conference, IPEC-Niigata - ECCE Asia 2018*, pp. 1073–1079, 2018.

[35] M. Yaqoob, K. H. Loo, and Y. M. Lai, "Modeling the effect of dead-Time on the soft-switching characteristic of variable-frequency modulated series-resonant DAB converter," *2017 IEEE 18th Workshop on Control and Modeling for Power Electronics, COMPEL 2017*, 2017.

[36] Y. Xie, J. Sun, and J. S. Freudenberg, "Power flow characterization of a bidirectional galvanically isolated high-power DC/DC converter over a wide operating range," *IEEE Transactions on Power Electronics*, vol. 25, no. 1, pp. 54–66, 2010.

[37] B. Zhao, Q. Song, W. Liu, and Y. Sun, "Dead-time effect of the high-frequency isolated bidirectional full-bridge DC-DC converter: Compre-

hensive theoretical analysis and experimental verification," *IEEE Transactions on Power Electronics*, vol. 29, no. 4, pp. 1667–1680, 2014.
[38] L. Xue, M. Mu, D. Boroyevich, and P. Mattavelli, "The optimal design of GaN-based Dual Active Bridge for bi-directional Plug-IN Hybrid Electric Vehicle (PHEV) charger," *Conference Proceedings - IEEE Applied Power Electronics Conference and Exposition - APEC*, vol. 2015-May, no. May, pp. 602–608, 2015.
[39] L. Xue, D. Boroyevich, and P. Mattavelli, "Switching condition and loss modeling of GaN-based dual active bridge converter for PHEV charger," *Conference Proceedings - IEEE Applied Power Electronics Conference and Exposition - APEC*, vol. 2016-May, pp. 1315–1322, 2016.
[40] R. Gupta and V. Karthikeyan, "Zero circulating current modulation for isolated bidirectional dual active bridge DC/DC converter," *IET Power Electronics*, vol. 9, no. 7, pp. 1553–1561, 2016.
[41] B. Zhao, Q. Song, and W. Liu, "Power characterization of isolated bidirectional dual-active-bridge dc-dc converter with dual-phase-shift control," *IEEE Transactions on Power Electronics*, vol. 27, no. 9, pp. 4172–4176, 2012.
[42] GaN Systems Inc., "GN001 Application Guide Design with GaN Enhancement Mode HEMT," pp. 1–46, 2018. [Online]. Available: https://gansystems.com/design-center/application-notes/
[43] T. Daranagama, F. Udrea, T. Logan, and R. McMahon, "A performance comparison of SiC and Si devices in a bi-directional converter for distributed energy storage systems," *2016 IEEE 7th International Symposium on Power Electronics for Distributed Generation Systems, PEDG 2016*, vol. 00, no. c, pp. 1–8, 2016.
[44] T. Zhao and J. He, "An optimal switching pattern for 'SiC+Si' hybrid device based Voltage Source Converters," *Conference Proceedings - IEEE Applied Power Electronics Conference and Exposition - APEC*, vol. 2015-May, no. May, pp. 1276–1281, 2015.

MACIÀ CAPÓ-LLITERAS was born in Menorca, Spain, in 1990. He received the M.Sc. degree in Industrial Engineering from "Escola Tècnica Superior d'Enginyers Industrials de Barcelona – Universitat Politècnica de Catalunya" (UPC) in 2014. From 2014 he joined the CITCEA research center of UPC as a project engineer developing tasks focused on the design of power electronics converters. This area involves DAB converters for DC/DC isolation, V2G projects for EV, and controllers for light electric vehicles. His main research interest is the hardware design with new semiconductors' technologies and its control in EV and battery integration.

DANIEL HEREDERO-PERIS was born in Vilanova i la Geltrú, Spain, in 1985. He received the M.Sc. degree in Control Engineering and Ph.D. from the School of Industrial Engineering of Barcelona, Universitat Politècnica de Catalunya (UPC) in 2010 and 2017. Since 2010 he is working with Centre d'Innovació Tecnològica en Convertidors Estàtics i Accionaments (CITCEA-UPC) as a project engineer developing tasks focused in design of algorithms related to the control of gridconnected and standalone single/three-phase inverters, and V2G projects for EV. His main research interests are control of power electronics, microgrids and EVs.

FRANCISCO DÍAZ-GONZÁLEZ was born in Barcelona, Spain in 1983. He received the degree in industrial engineering from the School of Industrial Engineering of Barcelona, Universitat Politècnica de Catalunya (UPC), Barcelona, Spain, in 2009, and the Ph.D. degree in electrical engineering from the UPC in 2013. Since 2016, he has been with the UPC, Barcelona, Spain, where he is currently working as a Lecturer (Serra Húnter programme) and researcher on projects related to energy storage technologies and renewable-based generating systems. His research activity is in the Centre d'Innovació Tecnològica en Convertidors Estàtics i Accionaments (CITCEA-UPC). He is the author of 1 book on energy storage for power systems, more than 20 articles in peer-reviewed journals and international conferences and 1 patent.

MARC LLONCH-MASACHS was born in Terrassa, Spain, in 1978. He received the M.Sc. degree in Industrial Engineering from the Escola T'ecnica Superior d'Enginyeria Industrial de Barcelona (ETSEIB), Universitat Polit'ecnica de Catalunya (UPC) in 2014. Since 2014 he is working with Centre d'Innovació Tecnològica en Convertidors Estàtics i Accionaments (CITCEA-UPC) as a project engineer carrying out tasks focused in development of grid connected and stand alone converters for DERs and EVs. His main research interest is focused in the power electronic knowledge at the service of micro-grids and EVs.

DANIEL MONTESINOS-MIRACLE (S01-M08-SM12) was born in Barcelona, Spain, in 1975. He received the M.Sc. degree in Electrical Engineering from the Escola Tecnica Superior d'Enginyeria Industrial de Barcelona (ETSEIB), Universitat Politècnica de Catalunya (UPC), Barcelona, Spain, in 2000, and PhD degree from the Universitat Politecnica de Catalunya (UPC), in 2008. In 2001 he joined Salicru Electronics, S.A., Santa Maria de Palautordera, Spain, as a research and development engineer. Since 2001 he has been involved in the Centre d'Innovació Tecnològica en Convertidors Estàtics i Accionaments (CITCEA-UPC) as a research collaborator. In 2005 he becomes a lecturer at Electrical Engineering Department, Universitat Politecnica de Catalunya (UPC). Since 2012 he is an Associate Professor at UPC. In 2012, he has co-founded teknoCEA, a spin-off company providing components, systems and services for power electronics research and manufacturing. His primary research interests are power electronics, drives and green energy converters.